Received 17 September 2023; revised 6 November 2023; accepted 14 November 2023. Date of publication 20 November 2023; date of current version 30 January 2024.

Digital Object Identifier 10.1109/OJAP.2023.3334219

Bandwidth Enhancement of H-Plane MIMO Patch Antennas in Integrated Sensing and Communication Applications

LINA MA [1,2] (Graduate Student Member, IEEE), ZIJIAN SHAO [3] (Member, IEEE), JUN LAI [1,2] (Student Member, IEEE), CHANGZHAN GU [1,2] (Senior Member, IEEE), AND JUNFA MAO [1,2] (Fellow, IEEE)

[1]State Key Laboratory of Radio Frequency Heterogeneous Integration, Shanghai Jiao Tong University, Shanghai 200240, China

[2]MoE Key Laboratory of Artificial Intelligence, Shanghai Jiao Tong University, Shanghai 200240, China

[3]Department of Electrical and Computer Engineering, Princeton University, Princeton, NJ 08540, USA

CORRESPONDING AUTHOR: C. GU (e-mail: changzhan@sjtu.edu.cn)

This work was supported in part by the Natural Science Foundation of China under Grant 61831016 and Grant 62171277, and in part by the Shanghai Municipal Science and Technology Major Project under Grant 2021SHZDZX0102.

(Lina Ma and Zijian Shao contributed equally to this work.)

ABSTRACT In this paper, a low-cost compact decoupled bandwidth enhancement technique is proposed to address the high mutual coupling issue between wideband closely-spaced multiple-input and multiple-out (MIMO) patch antennas. The wideband decoupling property is realized by combining two decoupling circuits introduced by defected ground structure (DGS) and coplanar decoupling structure, respectively. An equivalent circuit is given to clarify the decoupling mechanism and provide physical insight. To validate the feasibility of the proposed design scheme, two prototypes of decoupled wideband patch arrays based on coplanar-fed and probe-fed schemes are simulated, fabricated, and measured in the 5.8 GHz ISM band, respectively. Experimental results show that for both of the two kinds of prototypes, the poor isolation can be improved from 10 dB to better than 20 dB within a wide-matched bandwidth of 10% under an extremely close edge-to-edge distance of 0.038 λ_0. In addition, systematic validation for radar sensing performance has been discussed by integrating the proposed antenna with the custom-designed radio frequency system. Moreover, the performance metrics of MIMO parameters and verification of extending to 1×4 antenna arrays are also discussed for both two basic feeding schemes. Compared with the two-element patch arrays, multi-element patch arrays maintain decent performance for isolation enhancement and wideband isolation bandwidth larger than 10%, indicating the proposed decoupling technique is promising for large-scale wideband MIMO systems in integrated sensing and communication applications (ISAC).

INDEX TERMS Patch antennas, wideband antennas, antenna decoupling, decoupled bandwidth enhancement, multiple-input and multiple-out (MIMO), radar sensing, integrated sensing and communication applications (ISAC).

I. INTRODUCTION

With the explosive improvement of radio technology, how to integrate the functions of sensing and communication is the goal of beyond 5G or even 6G wireless communication applications in future Internet of Things (IoT) [1], intelligent transportation systems (ITS) [2], and Internet of Vehicles (IoV) [3]. For this purpose, integrated sensing and communication (ISAC) technology has received growing attention from both academia and industries [4], [5]. To maximize the use of limited spectrum resources,

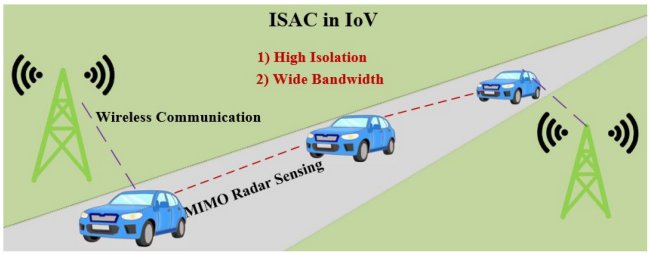

FIGURE 1. Illustration of a MIMO system for ISAC application.

multiple-input and multiple-output (MIMO) systems, which possess the merits of multiplexing gain, high transmission rate, huge data capacity, etc., have been widely used and drawn great attention in recent years [6], [7], [8], [9]. In MIMO antenna systems, the microstrip patch antenna is one of the most widely used types due to its compact low-profile appearance and easy-integrated characteristics. However, with the requirement for system miniaturization, especially in size-constrained applications, multiple antenna elements are required to be placed close to each other. As a result, strong mutual couplings inevitably exist between the adjacent units, which results in a large electromagnetic (EM) interference, and further leads to the deterioration of MIMO systems performance [8], [9]. Moreover, for radar sensing, the wider the operation bandwidth, the higher the resolution. Thus, how to find a compact and effective decoupling method to enlarge isolation between wideband MIMO elements is an urgent and significant problem to be solved. Multi-functional compact MIMO microstrip antenna with wide bandwidth and high isolation is highly expected in the ISAC scenario, as shown in Fig. 1.

A variety of decoupling techniques have been applied to eliminate the mutual coupling between narrow-band microstrip antennas, such as employing electromagnetic bandgap (EBG) [10] or split-ring resonators (SRR) [11], introducing a neutralization line [12], adding parasitic structures [13], and using decoupling feeding network [14]. In [10], EBG was first introduced to suppress the mutual coupling by 8 dB for array elements. In [13], a coplanar U-shape microstrip was inserted between two H-plane coupled patch elements to reduce the mutual coupling to below -30 dB within the operating band. In [14], a decoupling feeding network composed of two directional couplers was proposed to suppress the coupling between two patch elements to below -58 dB at the center frequency. Nevertheless, these methods [10], [11], [12], [13], [14] generally require a relatively large element spacing for decoupling. In addition to the above techniques, a coplanar strip wall [15], array-antenna decoupling surface (ADS) [16], metasurface-based decoupling method [17], and a dielectric block-based decoupling by controlling space-wave coupling to cancel surface-wave coupling [18] were also proposed for patch antenna decoupling. However, the techniques in [15], [16], [17], [18] require a high profile which is not favorable for a low-profile design.

Recently, some compact decoupling schemes are proposed to address the high mutual coupling between closely spaced microstrip patch antennas. In [19], a T-shape decoupling network was employed under the patch with an edge-to-edge space of less than 0.055 λ_0. In [20], a near-field resonator (NFR) was used as a coupling-mode transducer above each antenna element to achieve the isolation of better than 20 dB with small edge separations of 0.016 λ_0. In [21], by combing the DGS and metal via decoupling structure, good isolation was obtained for a 1×3 E-plane coupled patch array. In [22], through exploring the weakness field of the microstrip-fed patch, self-decoupling was realized without additional decoupling structure. In [23], Sun et al. proposed a general decoupling method based on a new perspective of CM and DM cancellation. With an extremely close edge-to-edge distance of 0.016 λ_0, poor isolation was improved to better than 15.4 dB across 2.394-2.530 GHz. In [24], a decoupling structure originating from the phase shift concept was proposed to enhance the isolation from 7 to 18 dB under the edge-to-edge separation of only 0.027 λ_0. In [25], a modular decoupling technique was proposed to enlarge the isolation to 40 dB with the edge-to-edge distance of 0.018 λ_0 at 6 GHz. Nevertheless, all the above schemes generally suffer a narrow bandwidth.

To sum up, although scholars have proposed many decoupling techniques for patch antenna structures with superior performance, however, the existing schemes either operate in a narrow band or fail to meet the need for low-profile applications. To the best of the authors' knowledge, it is the first decoupling scheme in the open literature to suppress the strong coupling between closely-spaced wideband microstrip patch antennas without sacrificing the low-profile and fabrication cost. We propose a novel approach to realize wideband decoupling with low-profile and low cost for wideband patch antennas.

The rest of this paper is organized as follows. Section II describes the decoupling mechanism for wideband microstrip patch antennas. The analysis of an equivalent circuit for this mechanism is also given. The design guideline with some cases is proposed to illustrate the decoupling property for wideband microstrip patch antennas in detail. Section III reports the prototypes and experiment results of the proposed antennas, and a comparison table with other decoupling structures is presented to highlight the merits. Moreover, performance metrics of MIMO parameters and the verification of extending to 1×4 antenna arrays are also discussed. In addition, Section IV gives a systematic validation for radar sensing performance = by integrating the proposed antenna with the custom-designed radio frequency system. Finally, a simple conclusion is summarized in Section V.

The innovations and contributions of this work are listed below:

1. This work, for the first time, proposes a wide-band decoupling scheme to suppress the strong coupling between closely-spaced wideband microstrip patch antennas without sacrificing the low-profile and

fabrication cost. Although researchers have proposed many decoupling techniques for patch antennas, all of them either operate in a narrow band or fail to meet the need for low-profile applications [10], [11], [12], [13], [14], [15], [16], [17], [18], [19], [20], [21], [22], [23], [24], [25]. It's the research aim and core contribution of this work.

2. A novel wideband hybrid decoupling scheme combining DGS and coplanar decoupling structure for wideband microstrip antenna is proposed. A transmission-line model is developed to explain the decoupling mechanism and provide physical insight succinctly.
3. To illustrate the decoupling property for wideband microstrip patch antennas, the decoupling scheme is experimentally proved effective for both the probe-fed and coplanar-fed wideband patch antennas.
4. To characterize the MIMO operation, the performance metrics of MIMO parameters for both of the two basic feeding schemes are analyzed by both simulation and experiment.
5. To validate the feasibility of the proposed wideband decoupling scheme in large-scale wideband array applications, the verification of extending to 1×4 antenna arrays for both of the two basic feeding schemes is conducted by both simulation and experiment.
6. Systematic validation for radar sensing performance has been discussed by integrating the proposed antenna with the custom-designed radio frequency system.

II. DESIGN AND ANALYSIS OF THE WIDEBAND DECOUPLING STRUCTURE

A. EQUIVALENT CIRCUIT OF WIDEBAND DECOUPLING MECHANISM

As known, an effective method for bandwidth enhancement for a microstrip patch antenna is to construct a dual-resonance structure, where one of the resonances is provided by the structure of the antenna itself and the other one is produced by the feeding structure or non-radiating matching network [26]. Here, we transfer this idea to the patch antenna decoupling for enhancing isolation bandwidth. Two additional resonant structures are constructed to provide dual decoupling frequencies, respectively. By separating the dual decoupling frequencies properly, a wideband decoupling property can be achieved.

To verify this idea, a novel wideband decoupling scheme combining DGS and coplanar decoupling structure for wideband microstrip antenna is proposed. The geometry of the basic structure is shown in Fig. 2. The DGS is constructed on the ground plane at the center of two patch antennas, and the coplanar decoupling structure is symmetrically located near the radiation side of the upper two antennas. When the two antennas are closing extremely, the near-field coupling is predominant. For the DGS, a high impedance occurs when the slot resonates. By moving the resonance of the slot close to one operating frequency of the wideband patch antenna, the isolation between adjacent elements can be improved significantly. The coplanar decoupling structure can be regarded as an equivalent resonant circuit consisting of a transmission line with a small gap and a shorting pin. Similarly, the closer the resonant frequency of this structure is to the other operating frequency of the wideband microstrip antenna, the higher the isolation is.

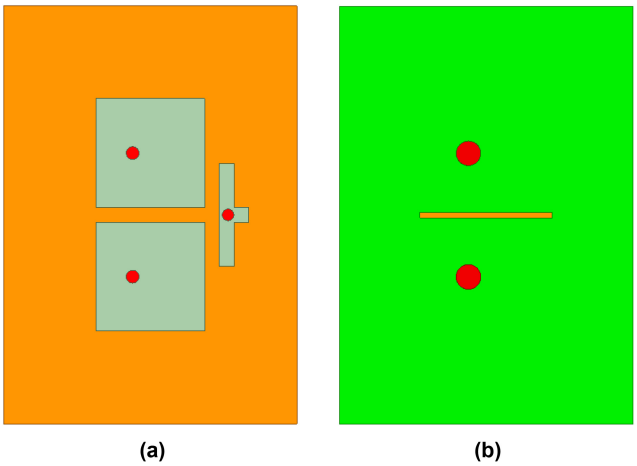

FIGURE 2. Schematic of (a) the top view and (b) the bottom view of the proposed wideband dual-decoupling structure.

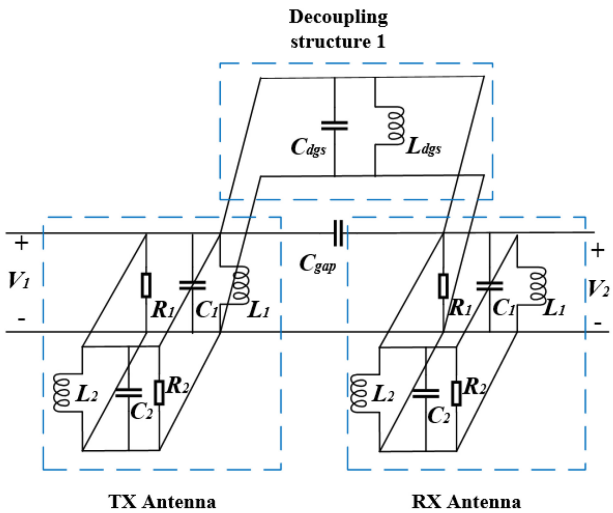

FIGURE 3. Equivalent circuit of DGS structure-based two-element wideband decoupling.

In order to analyze the broadband decoupling mechanism more intuitively, the equivalent circuit of the proposed wideband decoupling scheme is studied. First, we analyze the effect of DGS structure on isolation performance, and the simplified equivalent circuit is shown in Fig. 3. The equivalent circuit of the wideband antenna unit can be simplified to two parallel resonant circuits composed of R_1, L_1, and C_1, as well as R_2, L_2, and C_2, respectively. Meanwhile, the DGS structure can be simplified to a parallel circuit composed of L_{dgs}, and C_{dgs}.

For the original two-element model, we have

$$\begin{bmatrix} a_{21} & b_{21} \\ c_{21} & d_{21} \end{bmatrix} = \begin{bmatrix} 1 & \frac{1}{i\omega c_{gap}} \\ 0 & 1 \end{bmatrix} \tag{1}$$

where ω is the radian frequency, and C_{gap} presents the coupling capacitance.

From $S_{21}^{original} = \frac{2}{A+B/Z_0+CZ_0+D}$, the coupled signal transmitted from antenna 1 to 2 can be marked as

$$S_{21}^{original} = \frac{2i\omega c_{gap} Z_0}{2i\omega c_{gap} Z_0 + 1} \tag{2}$$

For the DGS structure, we have

$$\begin{bmatrix} a_{21} & b_{21} \\ c_{21} & d_{21} \end{bmatrix} = \begin{bmatrix} 1 & 0 \\ \frac{i\omega L_{dgs}}{1-\omega^2 L_{dgs} C_{dgs}} & 1 \end{bmatrix} \tag{3}$$

By converting the two-port transmission matrix to S-matrix, we get the following equation

$$S_{21}^{decoupling1} = \frac{2 - 2\omega^2 L_{dgs} C_{dgs}}{2 - 2\omega^2 L_{dgs} C_{dgs} + i\omega L_{dgs} Z_0} \tag{4}$$

To satisfy complete cancellation at the decoupling point, the amplitude and phase of the coupled signal at the decoupling point should meet

$$|S_{21}^{original}| = |S_{21}^{decoupling1}| \tag{5}$$

$$\angle S_{21}^{original} = \angle S_{21}^{decoupling1} + \pi \tag{6}$$

When the distance between the two antennas is determined, C_{gap} could be fixed. By changing the length and width of DGS, donated by L_{dgs} and W_{dgs}, the adjustment of decoupling frequency and cancellation amplitude about the decoupling circuit can be realized.

Similarly, the equivalent circuit model of the coplanar decoupling structure is shown in Fig. 4, where C_s represents the coupling capacitance between the antenna unit and the coplanar decoupling structure. The transmission line at both ends of the decoupling structure corresponds to a transmission line model with impedance Z_L and phase θ. The ground via in the middle of the transmission line is equivalent to a series circuit of L_{pin} and C_{sg}.

We divide the equivalent circuit model of the decoupling structure into five parts. For the decoupling structure, we get

$$\begin{bmatrix} a_1 & b_1 \\ c_1 & d_1 \end{bmatrix} = \begin{bmatrix} 1 & \frac{1}{i\omega c_s} \\ 0 & 1 \end{bmatrix} \tag{7a}$$

$$\begin{bmatrix} a_2 & b_2 \\ c_2 & d_2 \end{bmatrix} = \begin{bmatrix} \cos\theta & iZ_1 \sin\theta \\ \frac{i\sin\theta}{Z_1} & \cos\theta \end{bmatrix} \tag{7b}$$

$$\begin{bmatrix} a_3 & b_3 \\ c_3 & d_3 \end{bmatrix} = \begin{bmatrix} 1 & 0 \\ \frac{1}{i\omega L_{pin} + \frac{1}{i\omega c_{sg}}} & 1 \end{bmatrix} \tag{7c}$$

$$\begin{bmatrix} a_4 & b_4 \\ c_4 & d_4 \end{bmatrix} = \begin{bmatrix} \cos\theta & iZ_1 \sin\theta \\ \frac{i\sin\theta}{Z_1} & \cos\theta \end{bmatrix} \tag{7d}$$

$$\begin{bmatrix} a_5 & b_5 \\ c_5 & d_5 \end{bmatrix} = \begin{bmatrix} 1 & \frac{1}{i\omega c_s} \\ 0 & 1 \end{bmatrix} \tag{7e}$$

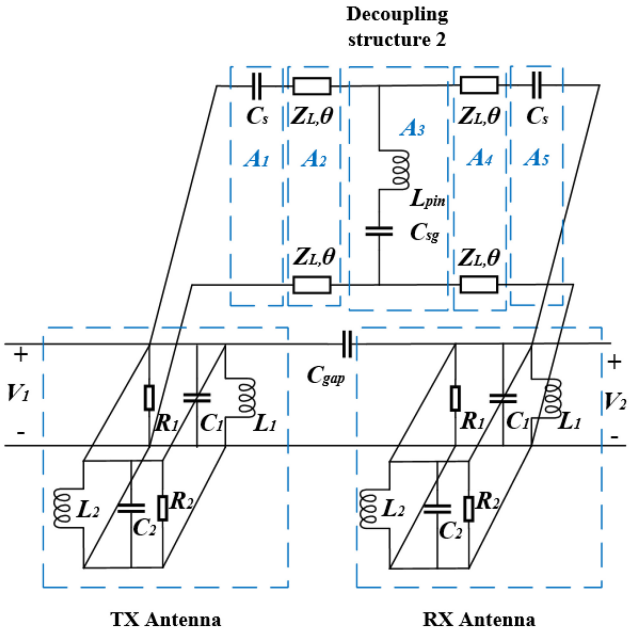

FIGURE 4. Equivalent circuit of coplanar decoupling structure-based two-element wideband decoupling.

After cascading, Eq. (7) can be expressed as

$$\begin{bmatrix} A & B \\ C & D \end{bmatrix} = \begin{bmatrix} a_1 & b_1 \\ c_1 & d_1 \end{bmatrix} \begin{bmatrix} a_2 & b_2 \\ c_2 & d_2 \end{bmatrix} \begin{bmatrix} a_3 & b_3 \\ c_3 & d_3 \end{bmatrix} \begin{bmatrix} a_4 & b_4 \\ c_4 & d_4 \end{bmatrix} \begin{bmatrix} a_5 & b_5 \\ c_5 & d_5 \end{bmatrix} \tag{8}$$

where

$$A = \cos 2\theta + \frac{i\sin\theta}{Z_1} + \frac{i\omega c_{sg}\cos\theta}{1-\omega^2 L_{pin} c_{sg}} \left(iZ_1 \sin\theta + \frac{\cos\theta}{i\omega c_s} \right) \tag{9a}$$

$$B = \frac{A}{i\omega c_s} + iZ_1 \cos\theta + \frac{\cos 2\theta}{i\omega c_s} - \frac{\omega c_{sg}\sin\theta}{1-\omega^2 L_{pin} c_{sg}} \left(iZ_1 \sin\theta + \frac{\cos\theta}{i\omega c_s} \right) \tag{9b}$$

$$C = \frac{i\sin 2\theta}{Z_1} + \frac{i\omega c_{sg}\cos\theta^2}{1-\omega^2 L_{pin} c_{sg}} \tag{9c}$$

$$D = \frac{C}{i\omega c_s} + \sin 2\theta - \frac{\omega c_{sg}\sin\theta}{1-\omega^2 L_{pin} c_{sg}} \tag{9d}$$

From $S_{21}^{decoupling2} = \frac{2}{A+B/Z_0+CZ_0+D}$, the decoupling signal transmitted from antenna 1 to 2 can be marked as

$$S_{21}^{decoupling2} = \frac{2i\omega^2 c_s Z_1 Z_0 \left(1-\omega^2 L_{pin} c_{sg}\right)}{E} \tag{10}$$

where

$$\begin{aligned} E = {} & \sin 2\theta - \omega^2 L_{pin} c_{sg} \sin 2\theta + 2i\omega c_s Z_0 \sin 2\theta \\ & - 2i\omega^3 L_{pin} c_{sg} c_s Z_0 \sin 2\theta - \omega^2 {c_s}^2 {Z_0}^2 \sin 2\theta \\ & + \omega^4 L_{pin} c_{sg} {c_s}^2 {Z_0}^2 \sin 2\theta + 2\omega c_s Z_1 \cos 2\theta \\ & - 2\omega^3 L_{pin} c_{sg} c_s Z_1 \cos 2\theta - \omega^2 {c_s}^2 {Z_1}^2 \sin 2\theta \\ & + \omega^4 L_{pin} c_{sg} {c_s}^2 {Z_1}^2 \sin 2\theta + 2i\omega^2 {c_s}^2 Z_0 Z_1 \cos 2\theta \\ & - 2\omega^4 L_{pin} c_{sg} {c_s}^2 Z_0 Z_1 \cos 2\theta - \omega^3 {c_s}^2 c_{sg} \cos\theta^2 {Z_0}^2 Z_1 \end{aligned}$$

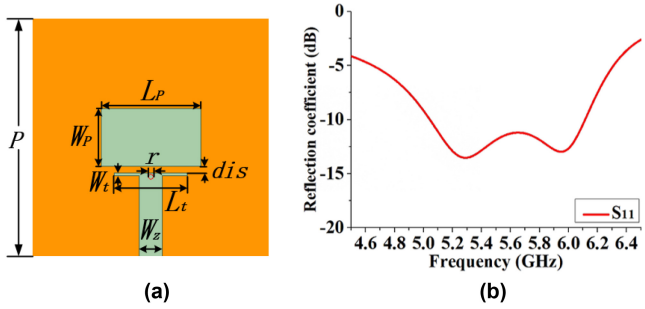

FIGURE 5. (a) Geometry and (b) Simulation S-parameter of coplanar-fed microstrip antenna. The detailed dimensions are: P=60 mm;L_p=14.5 mm; W_p=25 mm; dis=1.75 mm; L_t=18.5 mm; W_t=0.7 mm; W_z=5.8 mm; r=1. 2 mm.

$$+ i\omega^2 c_s c_{sg} Z_0 Z_1 \cos\theta^2 - i\omega^3 {c_s}^2 c_{sg} Z_0 {Z_1}^2 \sin\theta$$
$$- i\frac{1}{2}\omega^3 {c_s}^2 c_{sg} Z_0 {Z_1}^2 \sin 2\theta + \omega c_{sg} \cos\theta^2 Z_1$$
$$- \omega^3 {c_s}^2 c_{sg} {Z_1}^2 \sin\theta^2.$$

Similarly, at the decoupling point, it should satisfy

$$|S_{21}^{original}| = |S_{21}^{decoupling2}| \quad (11)$$
$$\angle S_{21}^{original} = \angle S_{21}^{decoupling2} + \pi \quad (12)$$

When C_{gap} is determined, by changing the length L_{de} and width W_{de} of the transmission line, the distance between the antenna unit and the decoupling structure d, the decoupling frequency and cancellation amplitude can be fine-tuned.

B. DECOUPLING BETWEEN TWO COPLANAR-FED H-PLANE CLOSELY SPACED WIDEBAND MICROSTRIP ANTENNAS

To validate the feasibility of the proposed design scheme, two basic types of microstrip antennas with coplanar feeding and probe feeding are investigated, respectively. In this part, the decoupling between two coplanar-fed wideband microstrip patch antennas is examined first.

Here, the coplanar-fed microstrip antenna in [26] is employed, whose geometry is shown in Fig. 5 (a). As seen, the microstrip patch and coplanar decoupling structure are designed on the top surface of a 3mm-thick F4B substrate ($\varepsilon_r = 2.2$, $\tan\delta = 0.001$). The corresponding simulated reflection coefficient of the coplanar-fed microstrip antenna is shown in Fig. 5 (b). It is seen that there are two resonant points, which correspond to the resonance frequency of the microstrip patch itself and the extra resonating circuit. The reflection coefficient of the antenna is lower than −10 dB across 5.05–6.11 GHz. In other words, the matching bandwidth of this antenna is about 19%.

Fig. 6 (a) shows the original configuration of a two-element coplanar-fed closely spaced H-plane microstrip antenna with an edge-to-edge distance of 2 mm (0.038 λ_0). The detailed dimensions of each element are the same as the unit designed before. The simulated reflection and transmission coefficients are shown in Fig. 6 (b). It reflects that the operating frequency range of the two patch antennas

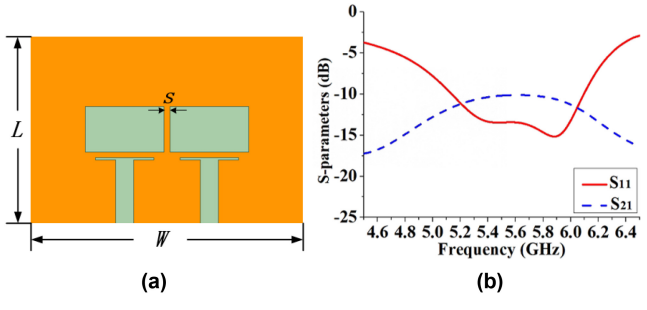

FIGURE 6. (a) Geometry and (b) Simulation reflection coefficient of original two-element coplanar-fed microstrip antennas. The detailed dimensions are: L=60 mm;W=87 mm; s=2 mm.

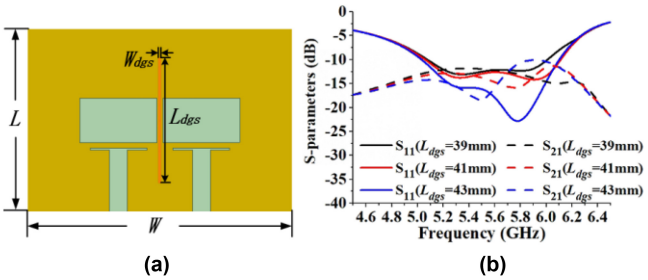

FIGURE 7. (a) Geometry and simulated S-parameters versus (b) L_{dgs} about coplanar-fed two-element closely spaced H-plane microstrip antennas with DGS only. The detailed dimensions are: L_{dgs}=41 mm; W_{dgs}=1 mm.

with $|S_{11}|/|S_{22}|$ lower than −10 dB is 5.14–6.09 GHz (the matching bandwidth of 17%), and the strong mutual coupling is up to 10 dB across the whole band.

To suppress the strong mutual coupling between these two antennas across the whole band, two decoupling structures are introduced to realize wideband decoupling. In order to illustrate the impact of each structure on the performance of isolation more intuitively, each decoupling structure is analyzed respectively.

Firstly, only DGS is added to the original configuration to introduce a decoupling network. The structure of two-element coplanar-fed H-plane coupled microstrip antennas with DGS is shown in Fig. 7 (a). The values of L, W and s in this structure are the same as those in Fig. 6 (a). To understand the proposed structure better, we have also performed parametric studies of this decoupling structure. It is found that the length of DGS L_{dgs} plays a key point in the decoupling performance. Fig. 7 (b) shows the S-parameters along with L_{dgs}. It can be seen that when L_{dgs}varies from 39 mm to 43 mm, the maximum isolations move down to different frequencies within the matching bandwidth. Meanwhile, the two resonant frequencies are almost unchanged. That's to say, by optimizing L_{dgs}, the decoupling frequency could be designed dependently without affecting the original resonance of the antenna.

Then, only the coplanar decoupling structure is applied to the original two-element antenna to introduce another decoupling circuit, as shown in Fig. 8 (a). Similarly, a parametric study has been conducted. According to the analysis above, there are four parameters - L_{de}, W_{de}, W_{pin},

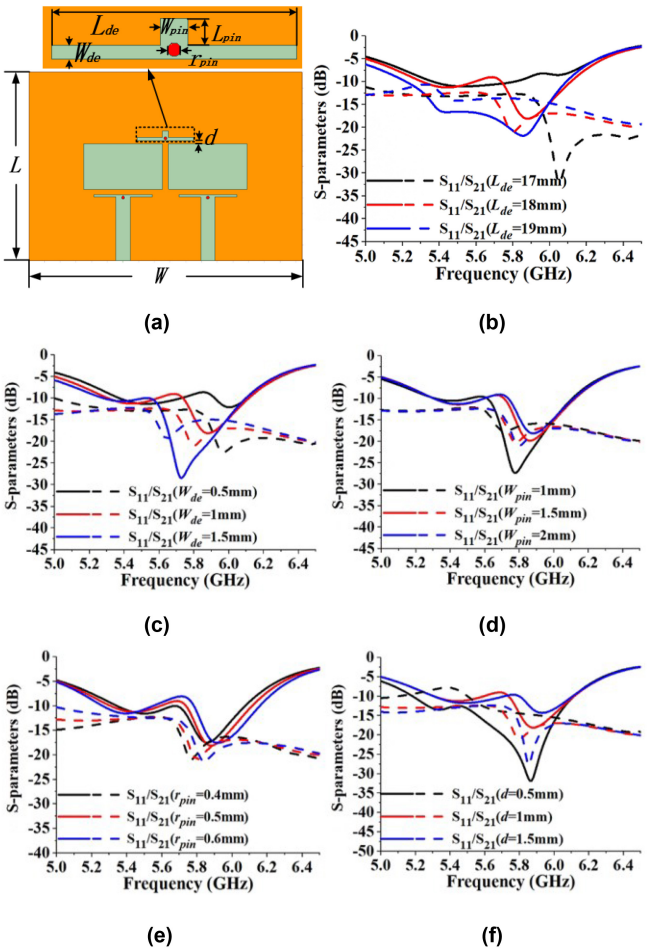

FIGURE 8. (a) Geometry and simulated S-parameter versus (b) L_{de}, (c) W_{de}, (d) W_{pin}, (e) r_{pin} and (f) d about coplanar coupling-fed two-element closely spaced H-plane microstrip antennas with coplanar decoupling structure only. The detailed dimensions are: L_{de}=18 mm; W_{de}=1 mm; d=1 mm; r_{pin}=1 mm; L_{pin}=W_{pin}=2 mm.

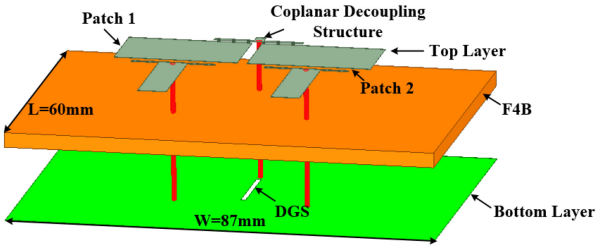

FIGURE 9. Exploded view of coplanar-fed two-element closely spaced H-plane microstrip antennas with dual-decoupling structure.

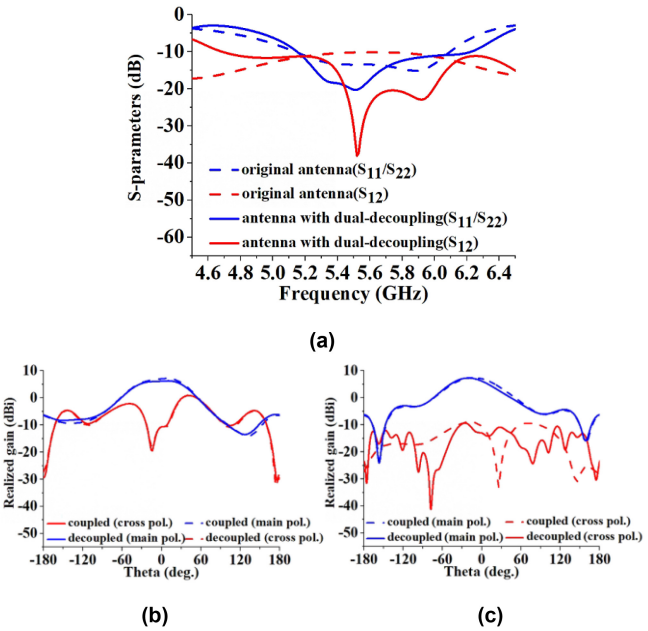

FIGURE 10. Comparison of (a) simulated S-parameters, patterns on (b) E plane and (c) H plane of coplanar-fed two-element closely spaced H-plane microstrip antennas with/without dual-decoupling structure.

r_{pin} and d, which affect the performance of impedance matching and decoupling capability. The S-parameters along with these parameters are shown in Figs. 8 (b)-(f). From Figs. 8 (b), (c) and (d), it shows that the length of the decoupling branch, denoted by L_{de}, the width of the decoupling branch W_{de} and the width of ground probe W_{pin}, can control the decoupling frequency of the structure. When L_{de} varies from 17 mm to 19 mm, the corresponding decoupling frequency keeps moving down. The smaller the length is, the stronger the magnitude will be. Similarly, as W_{de} or W_{pin} increases, the resonant frequency decreases sequentially. Meanwhile, the smaller W_{de} or W_{pin} is, the higher impedance will be. Fig. 8 (e) shows the relationship between the radius of via r_{pin} and the decoupling frequency of the structure. The smaller the radius is, the lower the resonant and the decoupling frequency is. The distance between the patch antennas and the coplanar decoupling structure d also affects the impedance and coupled energy of the decoupling structure. The simulated S-parameters of the two-element antenna versus different d are presented in Fig. 8 (f). When d increases, the decoupling frequency is shifted up accordingly. The larger the distance is, the stronger the magnitude will be. In a word, the isolation of this structure is sensitive to these five parameters. Among these parameters, L_{de} has the greatest effect on the S-parameters of a two-element antenna.

By simulating and analyzing the above two decoupling structures separately, the decoupling frequency and amplitude of each structure could be adjusted independently. Thus, the above investigations reveal that the wideband decoupling conditions in (5), (6), (11) and (12) can be readily achieved by properly tuning the dimensions of these two decoupling structures. Compared to the DGS, the coplanar decoupling structure has more design freedoms to satisfy the decoupling condition. Once these two decoupling frequencies have a suitable separation, a wideband decoupling can be achieved.

To further verify the wideband decoupling mechanism, in this part, a wideband decoupling technique, which combines DGS and coplanar decoupling structure is proposed. The detail structure scheme is illustrated in Fig. 9. A comparison of the simulated results without/with the decoupling structures is presented in Fig. 10. Fig. 10 (a) shows that the

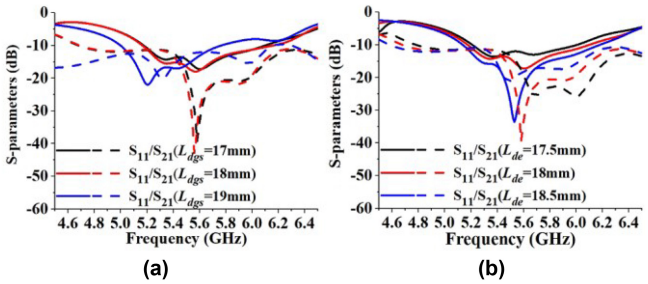

FIGURE 11. Simulated S-parameters versus (a) L_{dgs}, and (b) L_{de} about coplanar-fed two-element closely spaced H-plane microstrip antennas with dual-decoupling structure.

TABLE 1. Dimensions of the proposed antenna shown in Fig. 9. (Unit: mm).

Parameters	Dimensions	Parameters	Dimensions
L	60	W	87
L_p	14.5	W_p	25
L_t	18.5	W_t	0.7
W_z	5.8	dis	1.75
r	1.2	L_{dgs}	17
W_{dgs}	1	d	1
L_{de}	18	W_{de}	1
r_{pin}	1	W_{pin}	2

reflection coefficients of the proposed antenna are lower than −10 dB across 5.15–6.22 GHz. In other words, the matching impendence bandwidths of the proposed antenna are larger than 18.8%. Besides, it illustrates that the introduction of a decoupling structure hardly affects the impedance matching. Compared to the original two-element array without any decoupling structure, the isolation between the antenna element is enhanced from 10 dB to more than 20 dB obviously across 5.45–6 GHz with the maximum isolation reaching 40 dB at 5.55 GHz. The isolation bandwidth of 20 dB also achieves 9.6%. Fig. 10 (b) and (c) indicate that the existence of a dual-decoupling structure does not affect the radiation patterns.

Besides, the simulated S-parameters of the proposed scheme versus different L_{dgs} and L_{de} are presented in Fig. 10. Fig. 11 (a) shows that when L_{dgs} varies from 17 mm to 19 mm, the lower decoupling frequency is shifted down, which corresponds to the DGS decoupling structure. It also makes an explanation that the decoupling frequency of DGS can be adjusted independently without affecting the coplanar decoupling structure. Fig. 11 (b) shows that when L_{de} varies from 17.5 mm to 18.5 mm, the upper decoupling frequency is mainly shifted up. However, the lower decoupling frequency will move up accordingly. Thus, the above analysis simply reveals that the decoupling effect can be obtained by optimizing the dimensions of the decoupling structures, as tabulated in Table 1.

To give a better understanding of the decoupling performance of the proposed technique, the surface current

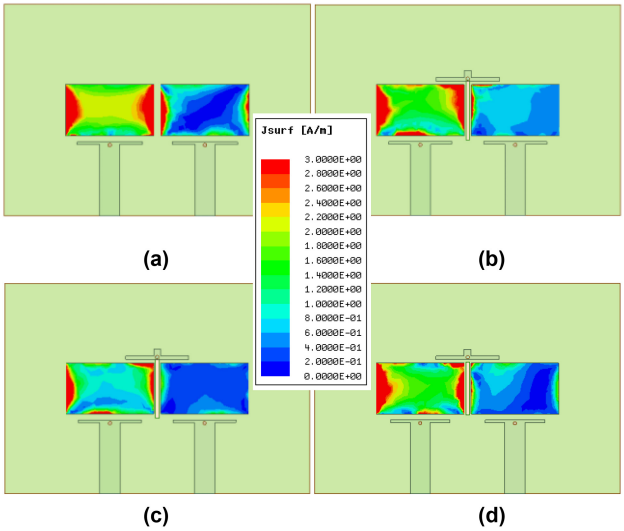

FIGURE 12. Comparison of the current distributions for different cases. (a) The original two-element antennas without dual-decoupling structure at 5.6 GHz. The proposed wideband decoupling antennas at (b) 5.5 GHz; (c) 5.6 GHz; (d) 6 GHz.

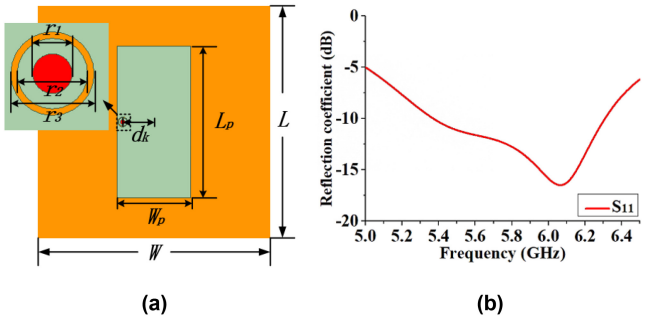

FIGURE 13. (a) Geometry and (b) simulation S-parameter of probe-fed microstrip antenna. The detailed dimensions are: L=W=45 mm; L_p=28 mm; W_p=14.2 mm; d_k=5.5 mm; r_1=1.3 mm; r_2=2.2 mm; r_3=2.5 mm.

distributions of the two-element array for different cases are depicted in Fig. 12. Fig. 12 (a) shows the surface current distribution of the original two-element antenna without any decoupling structures. When element 1 is excited, element 2 exhibits strong current distributions. After adding the decoupling structures, the surface current has been effectively suppressed across a wide operating bandwidth as shown in Figs. 12 (b)-(d). It is also noted that, when the antenna operates at 5.6 GHz, almost no current is witnessed on element 2, which corresponds to a peak isolation of 40 dB. From Fig. 12, it is revealed that the proposed decoupling structures successfully provide a remarkable decoupling effect.

C. DECOUPLING BETWEEN TWO PROBE-FED H-PLANE CLOSELY SPACED WIDEBAND MICROSTRIP ANTENNAS

The decoupling between two probe-fed wideband microstrip patch antennas is examined in this part. Similarly, a probe-fed microstrip antenna with wideband characteristics is designed in the first step, whose geometry is shown in Fig. 13 (a). As seen, a patch with a small annular gap is designed on

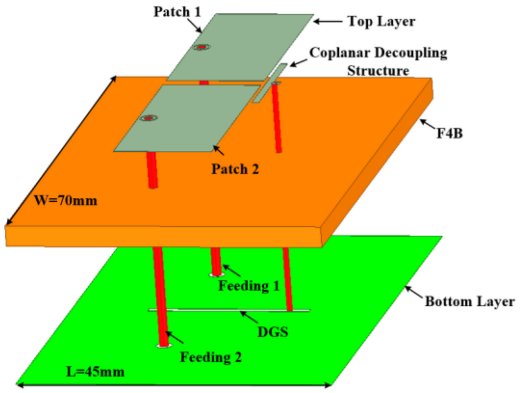

FIGURE 14. Exploded view of probe-fed two-element closely spaced H-plane microstrip antennas with dual-decoupling structure.

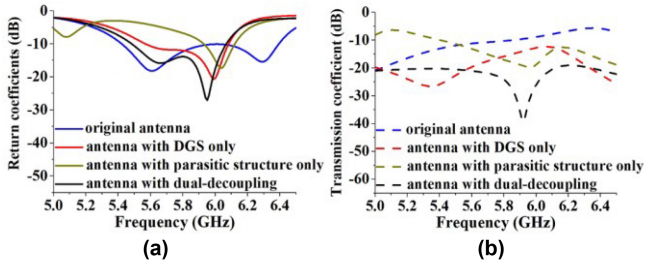

FIGURE 15. Comparison of simulated (a) |S11|/ |S22| and (b) |S12| of probe-fed two-element antennas without any decoupling structure, with DGS only, with parasitic structure only and with dual-decoupling structure.

the top surface of a 3mm-thick F4B substrate ($\varepsilon_r = 2.2$, $\tan\delta = 0.001$). In this structure, the small annular gap is used to provide a capacitance value. Combined with the vias, which is characterized by inductance, the other resonant circuit is formed to enlarge the impendence bandwidth. The corresponding simulated S-parameter of the probe-fed patch antenna is shown in Fig. 13 (b). It can be seen that there are two resonant points, which are offered by the microstrip patch itself and the extra resonating circuit from the probe and the annular gap, respectively. By constructing a dual-resonance structure, the characteristics of wideband are realized. The $|S_{11}|$ of the antenna is lower than –10 dB across 5.37-6.04 GHz, which indicates the impendence bandwidth of this antenna is larger than 11.7%.

Fig. 14 shows the wideband decoupling structure for a two-element probe-fed array based on the technique described before. Similarly, A comparison of the simulated results without/with the decoupling structures is presented in Fig. 15. After adding the wideband decoupling structures, the $|S_{11}|$ of the proposed antenna is all lower than –10 dB across the 5.48-6.07 GHz frequency range. In addition, the isolation between two-element antenna has been enlarged from 7 dB to 20 dB across the whole band with the maximum isolation reaching 40 dB at 5.92 GHz. The bandwidth of isolation is about 10.2%. The simulated results not only demonstrate the broadband decoupling properties of the proposed scheme but also illustrate the flexibility of the design under different feeding schemes.

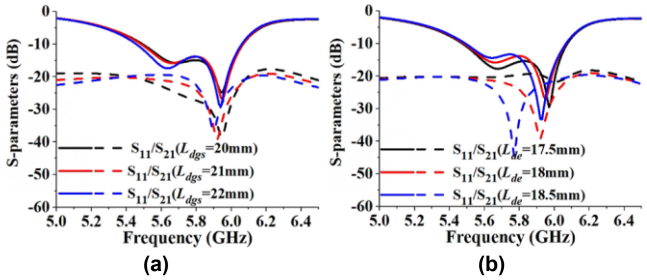

FIGURE 16. Simulated S-parameters versus (a) L_{dgs}, and (b) L_{de} about probe-fed two-element closely spaced H-plane microstrip antennas with dual-decoupling structure.

TABLE 2. Dimensions of the proposed antenna shown in Fig. 14. (Unit: mm).

Parameters	Dimensions	Parameters	Dimensions
L	45	W	70
L_p	28	W_p	14.2
r_1	1.3	r_2	2.2
r_3	2.5	d_k	5.5
L_{dgs}	21	W_{dgs}	1
L_{de}	18	W_{de}	1
d	0.5	W_{pin}	1
r_{pin}	0.8		

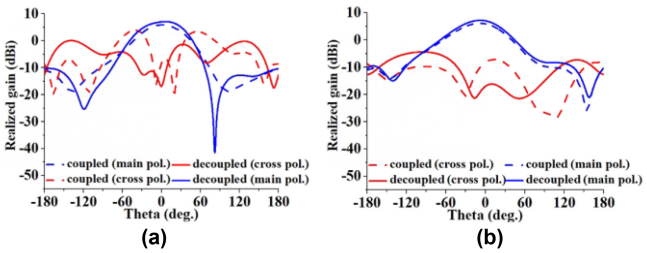

FIGURE 17. Comparison of simulated patterns on (a) E plane and (b) H plane of probe-fed two-element antennas without/with dual-decoupling structure.

The simulated S-parameters of the proposed scheme versus different important parameters, denoted by L_{dgs} and L_{de} are presented in Fig. 16. As seen, both the resonant frequency and isolation can be tuned by L_{dgs} and L_{de}. The final dimensions of the proposed antenna are tabulated in Table 2.

Fig. 17 gives a comparison of the simulated radiation patterns of the proposed probe-fed antenna without/with the decoupling structures. It shows clearly that after adding hybrid decoupling structures, the main-polarization radiation patterns are almost unaffected. It is noted that the cross-polarization levels have been improved.

III. PROTOTYPE AND MEASUREMENT RESULTS

A. MEASUREMENTS OF THE PERFORMANCE OF TWO-ELEMENT ARRAY

To verify the feasibility of the design schemes, the designed wideband decoupled antenna arrays based on coplanar-fed

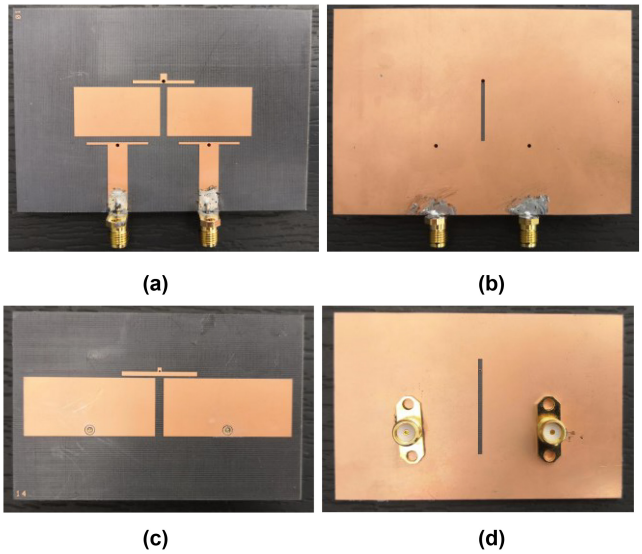

FIGURE 18. The (a) top view and (b) bottom view of the implemented coplanar -fed two-element microstrip antennas. The (c) top view and (d) bottom view of the implemented probe-fed two-element microstrip antennas.

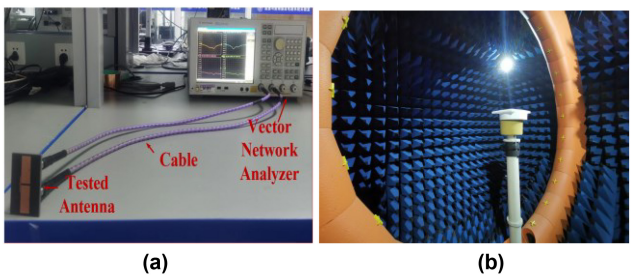

FIGURE 19. The experimental setup and scene. (a) Laboratory environment for impedance characteristic measurements. (b) Near-field chamber environment for radiation characteristic measurements.

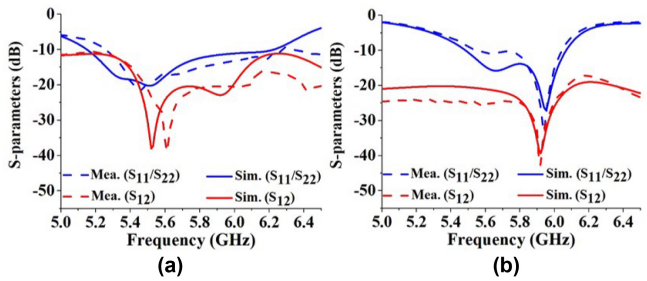

FIGURE 20. Simulated and measured S-parameters of (a) coplanar-fed two-element microstrip antennas, and (b) probe-fed two-element microstrip antennas.

and probe-fed schemes are fabricated and measured, respectively. The prototypes of the proposed antennas are shown in Fig. 18. The experimental setups and scenes are shown in Fig. 19. The two-port antenna array is connected to a calibrated vector network analyzer (VNA) by two SMA connectors. The Agilent network analyzer E5071C was employed for measuring the S-parameters and the radiation patterns were measured in a near-field chamber.

The simulated and measured S-parameters of the proposed antennas are shown in Fig. 20. Fig. 20 (a) reveals that the

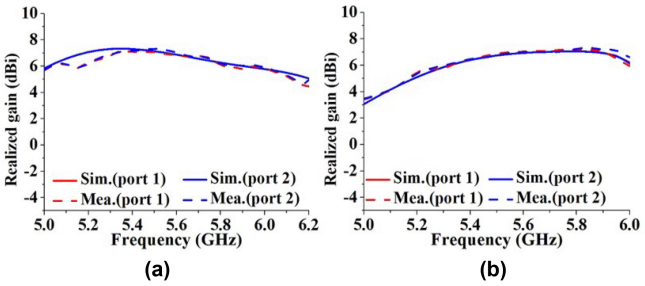

FIGURE 21. Simulated and measured realized gains of (a) coplanar-fed two-element microstrip antennas, and (b) probe-fed two-element microstrip antennas.

simulated reflection coefficients of the proposed coplanar-fed antenna are lower than −10 dB across 5.15–6.22 GHz, whose matching impendence bandwidths are larger than 18.8%. The isolation between two elements of the proposed antenna across 5.45–6 GHz has been enlarged from 10 dB to more than 20 dB obviously, whose 20 dB isolation bandwidth is up to 9.6%. Meanwhile, the maximum isolation is enhanced to 40 dB at 5.55 GHz. The corresponding measured reflection coefficients are all lower than −10 dB across 5.25–6.3 GHz, whose matching impedance bandwidths are up to 18.1%. The measured 20 dB isolation bandwidth between the two elements of the proposed antenna is up to 10.2% (from 5.49 GHz to 6.08 GHz). Meanwhile, the maximum isolation is up to 41 dB at 5.61 GHz. The little differences between the simulated and measured S-parameter levels are attributed to the small imperfections in the fabrication and assembling of the antenna as well as the welding level. Fig. 20 (b) shows that the reflection coefficients of the proposed probe-fed antenna are lower than −10 dB across 5.48–6.07 GHz, whose matching impendence bandwidths are larger than 10.7%. The isolation between the two-element antenna of the proposed array across the −10 dB operating bandwidth has been enlarged from 8 dB to better than 20 dB obviously, whose 20 dB isolation bandwidth is up to 10.7%. Meanwhile, the maximum isolation is enhanced to 40 dB at 5.92 GHz. The corresponding measured reflection coefficients are all lower than −10 dB across 5.48–6.06 GHz, whose matching impendence bandwidths are up to 10%. The measured 20 dB isolation bandwidth between the two-element antenna of the proposed array is up to 10%. Meanwhile, the maximum isolation is up to 43 dB at 5.92 GHz. Simulation and measured results show good agreement, which proves the feasibility of this design methodology.

The simulated and measured results of realized gains are shown in Fig. 21. As seen in Fig. 21 (a), the simulated and measured coplanar-fed antennas have realized gains of 5-7.3 dBi and 4.4-7.37 dBi for the probe-fed one within the 5.15-6.22 GHz and 5.25-6.3 GHz, respectively. Simulated and measured 1-dB gain bandwidth of the designed antenna are more than 570 MHz and 600 MHz. As seen in Fig. 21 (b), the simulated and measured probe-fed antennas have realized gains of 4.5–7.1 dBi and 4.9–7.36 dBi in 4.85–6.07 GHz and 5.5-6.06 GHz ISM band,

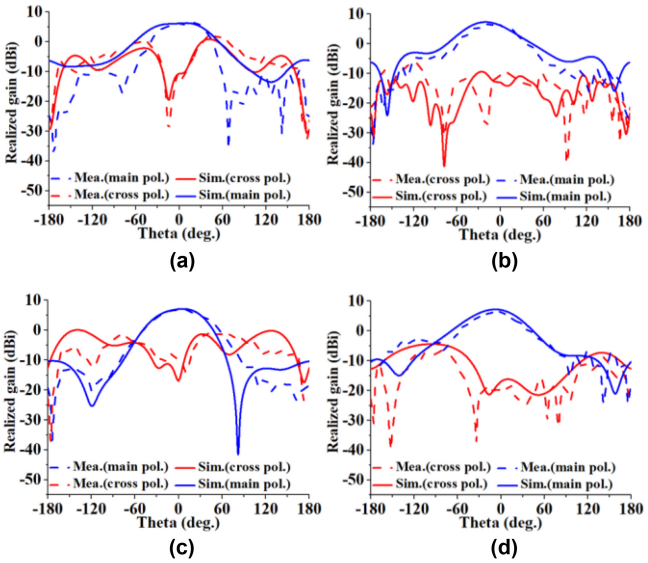

FIGURE 22. Simulated and measured radiation patterns of antenna element at 5.8 GHz. Patterns on (a) E plane and (b) H plane of coplanar-fed two-element microstrip antennas. Patterns on (c) E plane and (d) H plane of probe-fed two-element microstrip antennas.

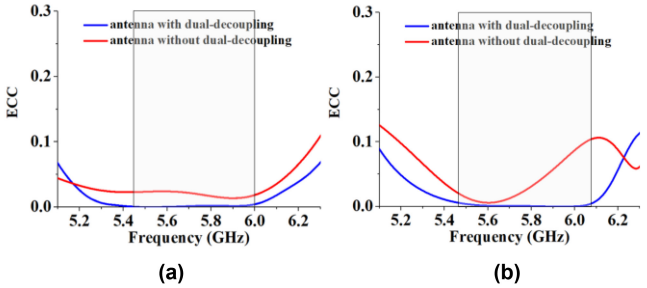

FIGURE 23. Comparison of simulated ECCs of (a) coplanar-fed and (b) probe-fed two-element microstrip antennas with/without dual-decoupling structure.

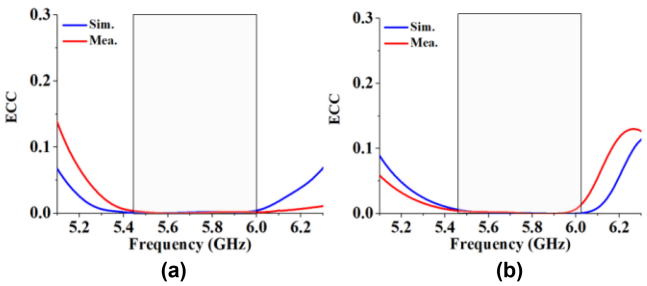

FIGURE 24. Simulated and measured ECCs of (a) coplanar-fed and (b) probe-fed two-element microstrip antennas.

respectively. Simulated and measured 1 dB gain bandwidth of the designed antenna are more than 540 MHz and 500 MHz.

The simulated and measured radiation patterns at 5.8 GHz are shown in Fig. 22. Since the two-element array is highly symmetrical, only radiation patterns of one port are given here. For the coplanar-fed antennas, the simulated and measured gains at the line of sight are 6.5 dBi and 6.3 dBi, respectively. Besides, the simulated and measured cross-polarization levels are −18 dB and −16 dB at the boresight direction, respectively. In the H-plane, the radiation pattern is symmetric. In the E-plane, the radiation pattern exhibits a slightly asymmetric shape, because of the little parasitic effect between two elements. The simulated and measured radiation efficiency of this kind of antenna is up to 96.8% and 88.2% respectively. For the probe-fed antennas, the simulated and measured gains at the boresight are 7.1 dBi and 7 dBi, respectively. In addition, the simulated and measured cross-polarization levels are −23 dB and −17 dB in the boresight direction, respectively. Note that the radiation patterns are basically symmetrical in the H-plane and slightly asymmetrical in the E-plane due to the little parasitic effect. The simulated and measured radiation efficiency is up to 93.6% and 85.8% respectively.

B. PERFORMANCE EVALUATION OF MIMO PARAMETERS

For proper MIMO characterization, the description of other key MIMO parameters, such as envelope correlation coefficient (ECC), total active reflection coefficient (TARC), mean effective gain (MEG), and diversity gain (DG), channel capacity has also been mentioned in our work.

The ECC is a key parameter for MIMO antennas since it has an effect on the loss of radiation efficiency and performance of MIMO systems. The acceptable ECC is less than 0.5 normally [27].

The comparison of simulated ECC for two kinds of the proposed antenna with/without the proposed decoupling scheme is plotted in Fig. 23. It indicates that after adding the proposed decoupling structure, ECCs have been reduced from 0.03 to 0.004, which is much lower than the acceptable value. The simulated and measured ECC curves are plotted in Fig. 24. Good agreement is observed between the simulated and measured curves. For two two-element patch antennas, both the simulated and measured ECCs are below 0.004 across the whole operating band.

TARC is another important parameter that must also be considered. The lower the TARC is, the smaller the impact on channel capacity. Take the 2×2 antenna arrays as an example. TARC can be described as [28]

$$\Gamma_a^t = \frac{\sqrt{\left(|(s_{11}+s_{12})|^2+|(s_{21}+s_{22})|^2\right)}}{\sqrt{2}} \tag{13}$$

The simulated and measured TARCs curves are plotted in Fig. 25. The values retain the original behavior of a single antenna characteristic.

MEG is a real index of antenna gain characteristics. In mobile communication, the MEG is usually repressed by [29]

$$G_e = \int_0^{2\pi}\int_0^{\pi}\left\{\frac{XPR}{1+XPR}G_\theta(\theta,\varphi)P_\theta(\theta,\varphi) + \frac{1}{1+XPR}G_\varphi(\theta,\varphi)P_\varphi(\theta,\varphi)\right\}\sin\theta d\theta d\varphi \tag{14}$$

where XPR means cross-polarization power ratio and equals to P_1/P_2. P_1 and P_2 are the mean power received by

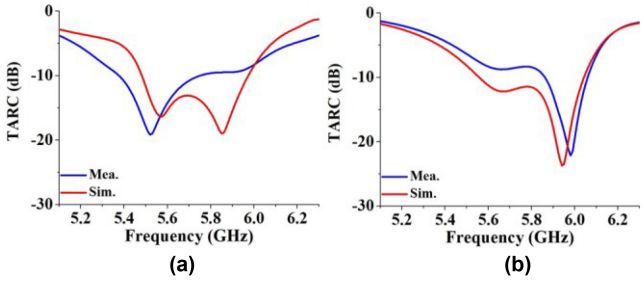

FIGURE 25. Simulated and measured TARCs of (a) coplanar-fed and (b) probe-fed two-element microstrip antennas.

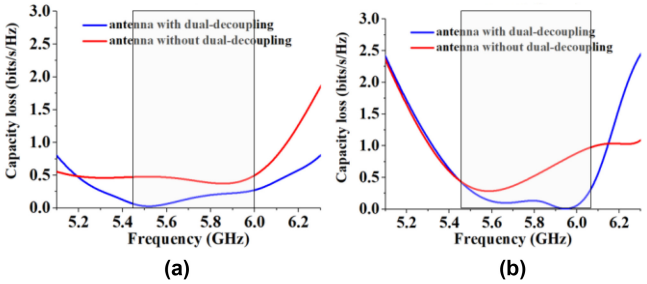

FIGURE 26. Comparison of simulated capacity losses of (a) coplanar-fed and (b) probe-fed two-element closely spaced H-plane microstrip antennas.

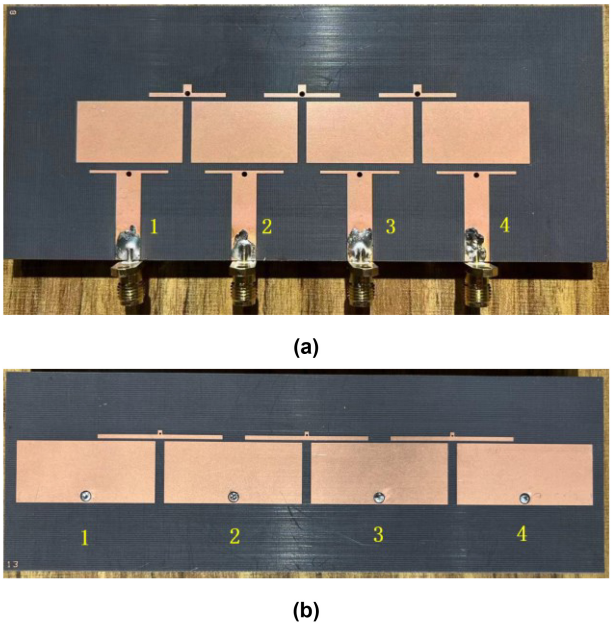

FIGURE 27. Fabricated prototypes of the proposed extremely closely spaced 1 × 4 antenna arrays based on (a) coplanar-fed and (b) probe-fed.

vertically and horizontally polarized isotropic antennas in a multipath environment. G_θ and G_φ are the θ and φ components of power gain pattern of the receiving antenna. P_θ and $P_\varphi$are the θ and φ components of the angular density functions of incoming plane waves. The higher MEG reflects the good match between the antenna and the channel, which enables the channel to receive more signal power.

The incident radio wave parameters are determined to be typical values in urban areas. Here, the XPR is fixed as 6 dB, the mean elevation angles are from 0 to 40°, and the standard deviation is 20°. For the coplanar-fed patch antenna, the simulated and measured MEGs at 5.8 GHz are 8.6 dBi and 8.22 dBi in the boresight, respectively. For the probe-fed patch antenna, the simulated and measured MEGs at 5.8 GHz are 8.1 dBi and 7.82 dBi in the boresight, respectively.

DG provides an enhancement in the system with several antennas compared to a system with a single antenna [30]. The higher the DG, the better the communication quality. Take the 2×2 antenna arrays at a 1% cumulative probability level as an example. For the coplanar-fed patch antenna, the simulated and measured DGs at 5.8 GHz are 9.39 dBi and 9.28 dBi in the boresight, respectively. For the probe-fed patch antenna, the simulated and measured DGs at 5.8 GHz are 9.15 dBi and 9.02 dBi in the boresight, respectively.

Theoretically, the capacity of the MIMO system grows linearly with the number of antennas. However, the ECC in the MIMO channel induces a loss of capacity. For the same MIMO system, channel capacity can be characterized by capacity loss indirectly. Take the 2×2 antenna arrays as an example. The channel capacity loss of the antenna can be calculated by [31]

$$C_{loss} = -\log_2 \det(\varphi_R) \tag{15}$$

where $\varphi_R = \rho_{ij}(i, j = 1, 2)$ represents the correlation matrix. The elements are determined from the formula $\rho_{ij} = -S_{ii}^* S_{ij} - S_{ji}^* S_{jj}$ and $\rho_{ii} = 1 - |S_{ii}|^2 - |S_{ij}|^2 (i, j = 1, 2)$. Thus, the channel capacity losses curves of the antennas with/without the decoupling structure across the operating band can be plotted in Fig. 26. It indicates that after adding the proposed decoupling structure, capacity losses have been much reduced across the whole operating band.

C. COMPARISON WITH OTHER DECOUPLING STRUCTURES

To highlight the merits of the proposed decoupling scheme, a comparison between our decoupling scheme and some other decoupling closely spaced patch antennas is shown in Table 3. It can be seen that our designs provide a much wider decoupled operating bandwidth as compared with most of the other works. Although the structure in [18] has a larger decoupled bandwidth, it suffers a high profile and increased fabrication cost for an additional substrate layer. Moreover, the proposed decoupling technique possesses the advantages of extremely closely spaced (edge-to-edge distance of 0.038 λ_0), high isolation (the maximum value up to 41 dB), wide 20 dB isolation bandwidth (up to 10.2%), high gain (up to 7.37 dBi), and wide 1 dB gain bandwidth (up to 9.2%).

D. EXTENSION TO 1×4 ANTENNA ARRAYS

To validate the feasibility of the proposed wideband decoupling scheme in large-scale wideband array applications, the verification of extending to 1×4 antenna arrays is also discussed. Fig. 27 shows the fabricated prototypes of

TABLE 3. Comparison between this work and existing decoupling schemes for patch antennas.

Ref.	Decoupling Schemes	Array Config.	Single-Layer Fabrication	Profile (λ_0) [a]	ES [b] (λ_0)	-10 dB Impedance BW	Isolation (dB)	20 dB Isolation BW [c]	Maximum Gain (dBi)	1-dB gain BW
[15]	Asymmetrical coplanar strip wall	H-plane	Yes	0.15 ↑	0.03	1.3%	35-45	1.3%	NG	NG
[16]	Array-antenna decoupling surface	H-plane	No	0.31 ↑	0.082	~4%	>24	~4%	NG	NG
[18]	Dielectric block Superstrate	E-Plane H-plane	No	0.42 ↑ 0.18 ↑	0.1 ↑ 0.027	14% ↑ 27.3% ↑	>20	14% ↑ 27.3% ↑	6.88 4.14	NG
[19]	Decoupling network	E-plane	No	0.056	0.056	~4%	24-33	~4%	5.6	NG
[20]	Near-Field Resonators	H-Plane E-Plane	No	0.088	0.024	6.1% 5.8%	20-30	6.1% 5.8%	NG	NG
[21]	DGS with metal vias	E-Plane	Yes	0.02	0.037	~2.5%	20-35	~2.5%	3.94	1.2%
[22]	Self-decoupling	E-Plane	Yes	0.037	0.18 ↑	2.8%	30-61	2.8%	7.1	NG
[23]	Mode-cancellation method	E-Plane	Yes	0.049	0.016	5.5%	15.4-16	-	7.8	5.5%
[24]	Parasitic structure	H-Plane	Yes	0.02	0.027	1.4%	18-20	-	5.5	1.4%
[25]	Parasitic structure	H-Plane	Yes	0.02	0.018	3.3%	30-40	3.3%	~5.2	3.3%
[32]	Microstrip lines	H-Plane	Yes	0.02	0.017	2.5%	22-30	2.5%	3.8	2.5%
[33]	Grounded stub	H-Plane	Yes	0.03	0.017	2.1%	20-38	2.1%	4.5	2.1%
This work Coplanar-fed	Parasitic structure with DGS	H-Plane	Yes	0.058	0.038	18.1% ↑	15-41	10.2% ↑	7.37	9.2%
This work Probe-fed	Parasitic structure with DGS	H-Plane	Yes	0.058	0.038	10% ↑	22-43	10% ↑	7.36	8.7%

[a]. λ_0 is the free-space wave length of the center frequency f_0. [b]. The ES refers to the edge-to-edge space. [c]. The 20 dB isolation BW refers to the -10 dB impedance bandwidth of isolation more than 20 dB.

the proposed antenna arrays based on coplanar feeding and probe feeding, respectively. The space distance and dimensions of the basic antenna are the same as that of the aforementioned two-element schemes, except for the number of units. Simulated and measured S-parameters of two kinds of proposed antenna arrays are shown in Figs. 28-29. Due to the isolations between non-adjacent elements being much larger than those between adjacent elements, these data are not shown for simplicity. For the coplanar-fed antenna array, the simulated and measured −10 dB impedance bandwidth of all elements is 16.4% (5.15–6.07 GHz) and 11.3% (5.33–5.97 GHz), respectively. The isolations between adjacent elements are successfully improved from 10 dB to better than 18 dB and 15 dB in the simulation and experiment, respectively. For the probe-fed antenna array, the

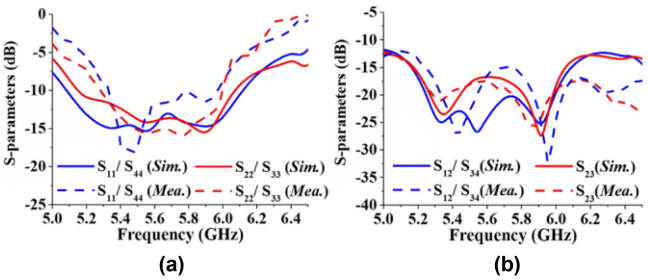

FIGURE 28. Simulated and measured S-parameters about coplanar-fed proposed 1×4 antenna arrays.

simulated and measured −10 dB impedance bandwidth of all elements is 10% (from 5.43 GHz to 6 GHz) and 10% (from 5.5 GHz to 6.08 GHz), respectively. The isolations between

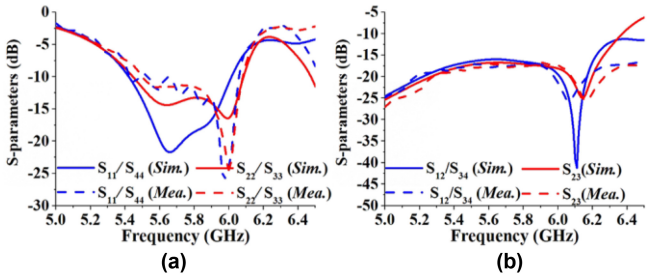

FIGURE 29. Simulated and measured S-parameters about probe-fed proposed 1×4 antenna arrays.

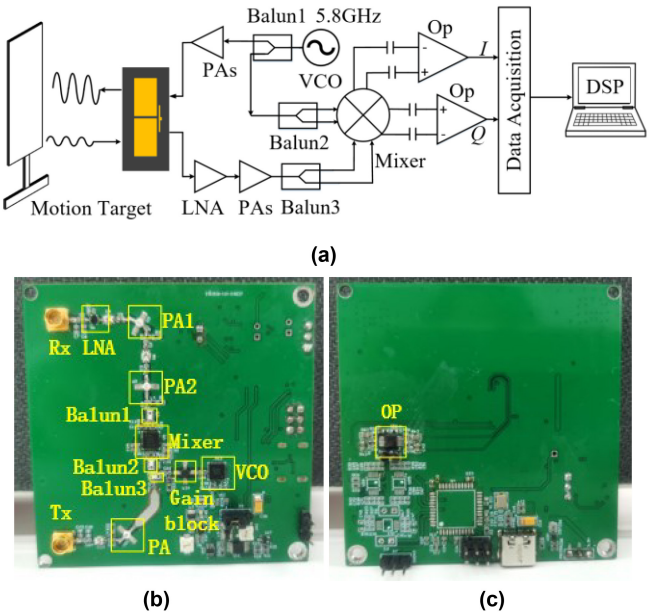

FIGURE 30. (a) The block diagram of measuring the motion of the actuator. (b) The top and (c) bottom view of the custom-designed 5.8 GHz radar system.

adjacent elements have been improved from 7 dB to better than 16.2 dB and 17.5 dB in the simulation and experiment, respectively. Compared with the two-element schemes, the isolation enhancement and isolation bandwidth for multi-element patch arrays show relatively stable performance, which indicates that the proposed technique is also feasible and practical for multi-element decoupling in wideband arrays.

IV. SENSING PERFORMANCE VERIFICATION

To evaluate the effectiveness of using the proposed design for ISAC, the designed probe-fed two-element microstrip antennas are integrated into a 5.8 GHz continuous wave radar system for detecting the motion of an actuator. The block diagram of the radar system with the proposed antennas is shown in Fig. 30. The details of the used components are listed in Table 4. The radar is set at a 30 cm distance apart to measure the motion of an actuator. The actuator is programmed to take a sinusoidal motion with a frequency of 1 Hz, and the amplitude of motion is set as 1 cm.

TABLE 4. Main devices used in the system.

Function	Company	Device	Specifications
Voltage-controlled oscillator	ADI	HMC431	Bandwidth: 5.5-6.1 GHz
Balun	TDK	HHM1562B	Bandwidth: 5.15-5.875 GHz
Power amplifier	Qorvo	NBB-400-T1	Bandwidth: DC-8 GHz; NF: 4.3 dB; Gain: 14.6 dB
Gain block	Mini-Circuits	ERA-9SM+	Bandwidth: DC-8 GHz; NF: 5 dB; Gain: 8.4 dB
Low noise amplifier	NXP	BGU7258	Bandwidth: 5.1-5.9 GHz; NF: 1.6 dB; Gain: 14 dB
Quadrature mixer	ADI	ADL5380	Bandwidth: 0.4-6 GHz; NF: 15.5 dB; Gain: 5.8 dB
IF amplifier	ADI	MAX9917	Gain Bandwidth: 1 MHz

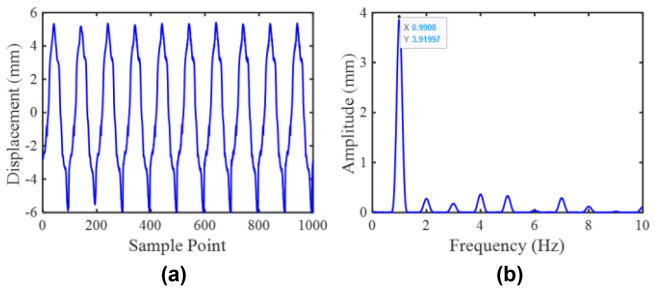

FIGURE 31. Experimental results of a periodic motion with a frequency of 1 Hz and a displacement of 1 cm. (a) Demodulated movement. (b) Spectrum after FFT.

The measured results are presented in Fig. 31. It shows clearly that due to the high mutual coupling suppression of the proposed antennas, the demodulated movement is basically the same as the setting data with almost no distortion and no leakage signals.

V. CONCLUSION

In this paper, a compact decoupled bandwidth enhancement scheme is proposed to address the mutual coupling issue between wideband patch antennas. A novel approach combining with both DGS and coplanar decoupling structures is proposed to realize the wideband decoupling property with a single-layer low-profile appearance. Two basic types of patch antennas based on coplanar-fed and probe-fed are examined with extremely close edge-to-edge distances of 0.038 λ_0, respectively. Experimental results demonstrate that for the coplanar-fed two-element patch antenna, the poor

isolation is improved from 10 dB to better than 20 dB across 5.49-6.08 GHz, and the maximum isolation is enhanced to 41 dB at 5.61 GHz. For the probe-fed two-element scheme, the poor isolation is improved from 6 dB to better than 22 dB across 5.48–6.06 GHz, and the maximum isolation is up to 43 dB at 5.92 GHz. Performance metrics of MIMO parameters have also been analyzed to characterize the MIMO operation. In addition, systematic validation for radar sensing performance has been discussed by integrating the proposed antenna with the custom-designed radar system. Besides, the 1×4 antenna arrays for both the two feeding schemes also perform at least 10% decoupled bandwidths with isolation larger than 15 dB for the worst condition. Owing to its compact appearance and single-layer simple structure, it is believed that the proposed decoupling scheme possesses an attractive potential for large-scale wideband MIMO systems in ISAC applications.

REFERENCES

[1] A. Zanella, N. Bui, A. Castellani, L. Vangelista, and M. Zorzi, "Internet of Things for smart cities," *IEEE Internet Things J.*, vol. 1, no. 1, pp. 22–32, Feb. 2014.

[2] J. Choi, V. Va, N. Gonzalez-Prelcic, R. Daniels, C. R. Bhat, and R. W. Heath, "Millimeter-wave vehicular communication to support massive automotive sensing," *IEEE Commun. Mag.*, vol. 54, no. 12, pp. 160–167, Dec. 2016.

[3] M. Tighezza, S. K. A. Rahim, and M. T. Islam, "Flexible wideband antenna for 5G applications," *Microw. Opt. Technol. Lett.*, vol. 60, no. 1, pp. 33–44, 2018.

[4] F. Liu et al., "Integrated sensing and communications: Toward dual-functional wireless networks for 6G and beyond," *IEEE J. Sel. Areas Commun.*, vol. 40, no. 6, pp. 1728–1767, Jun. 2022.

[5] J. Zhang, E. Björnson, M. Matthaiou, D. W. K. Ng, H. Yang, and D. J. Love, "Prospective multiple antenna technologies for beyond 5G," *IEEE J. Sel. Areas Commun.*, vol. 38, no. 8, pp. 1637–1660, Aug. 2020.

[6] A. O. Martínez, J. Ø. Nielsen, E. De Carvalho, and P. Popovski, "An experimental study of massive MIMO properties in 5G scenarios," *IEEE Trans. Antennas Propag.*, vol. 66, no. 12, pp. 7206–7215, Dec. 2018.

[7] Z. Ren, S. Wu, and A. Zhao, "Coexist design of sub-6 GHz and millimeter-wave antennas for 5G mobile terminals," in *Proc. Int. Symp. Antennas Propag.*, Busan, South Korea, 2018, pp. 805–806.

[8] F. Rusek et al., "Scaling up MIMO: Opportunities and challenges with very large arrays," *IEEE Signal Process. Mag.*, vol. 30, no. 1, pp. 40–60, Jan. 2013.

[9] T. Riihonen, D. Korpi, O. Rantula, H. Rantanen, T. Saarelainen, and M. Valkama, "Inband full-duplex radio transceivers: A paradigm shift in tactical communications and electronic warfare?" *IEEE Commun. Mag.*, vol. 55, no. 10, pp. 30–36, Oct. 2017.

[10] F. Yang and Y. Rahmat-Samii, "Microstrip antennas integrated with electromagnetic band-gap (EBG) structures: A low mutual coupling design for array applications," *IEEE Trans. Antennas Propag.*, vol. 51, no. 10, pp. 2936–2946, Oct. 2003.

[11] M. M. Bait-Suwailam, O. F. Siddiqui, and O. M. Ramahi, "Mutual coupling reduction between microstrip patch antennas using slotted complementary split-ring resonators," *IEEE Antennas Wireless Propag. Lett.*, vol. 9, pp. 876–878, 2010.

[12] A. Diallo, C. Luxey, P. Le Thuc, R. Staraj, and G. Kossiavas, "Study and reduction of the mutual coupling between two mobile phone PIFAs operating in the DCS1800 and UMTS bands," *IEEE Trans. Antennas Propag.*, vol. 54, no. 11, pp. 3063–3074, Nov. 2006.

[13] S. Farsi, H. Aliakbarian, D. Schreurs, B. Nauwelaers, and G. A. E. Vandenbosch, "Mutual coupling reduction between planar antennas by using a simple microstrip U-section," *IEEE Antennas Wireless Propag. Lett.*, vol. 11, pp. 1501–1503, 2012.

[14] R.-L. Xia, S.-W. Qu, P.-F. Li, Q. Jiang, and Z.-P. Nie, "An efficient decoupling feeding network for microstrip antenna array," *IEEE Antennas Wireless Propag. Lett.*, vol. 14, pp. 871–874, 2015.

[15] H. Qi, L. Liu, X. Yin, H. Zhao, and W. J. Kulesza, "Mutual coupling suppression between two closely spaced microstrip antennas with an asymmetrical coplanar strip wall," *IEEE Antennas Wireless Propag. Lett.*, vol. 15, pp. 191–194, 2016.

[16] K.-L. Wu, C. Wei, X. Mei, and Z.-Y. Zhang, "Array-antenna decoupling surface," *IEEE Trans. Antennas Propag.*, vol. 65, no. 12, pp. 6728–6738, Dec. 2017.

[17] F. Liu, J. Guo, L. Zhao, G.-L. Huang, Y. Li, and Y. Yin, "Dual-band metasurface-based decoupling method for two closely packed dual-band antennas," *IEEE Trans. Antennas Propag.*, vol. 68, no. 1, pp. 552–557, Jan. 2020.

[18] M. Li, M. Y. Jamal, L. Jiang, and K. L. Yeung, "Isolation enhancement for MIMO patch antennas sharing a common thick substrate: Using a dielectric block to control space-wave coupling to cancel surface-wave coupling," *IEEE Trans. Antennas Propag.*, vol. 69, no. 4, pp. 1853–1863, Apr. 2021.

[19] X.-J. Zou, G.-M. Wang, Y.-W. Wang, and H.-P. Li, "An efficient decoupling network between feeding points for multielement linear arrays," *IEEE Trans. Antennas Propag.*, vol. 67, no. 5, pp. 3101–3108, May 2019.

[20] M. Li, B. G. Zhong, and S. W. Cheung, "Isolation enhancement for MIMO patch antennas using near-field resonators as coupling-mode transducers," *IEEE Trans. Antennas Propag.*, vol. 67, no. 2, pp. 755–764, Feb. 2019.

[21] Z. Niu, H. Zhang, Q. Chen, and T. Zhong, "Isolation enhancement for 1×3 closely spaced E-plane patch antenna array using defect ground structure and metal-vias," *IEEE Access*, vol. 7, pp. 119375–119383, 2019.

[22] H. Lin, Q. Chen, Y. Ji, X. Yang, J. Wang, and L. Ge, "Weak-field-based self-decoupling patch antennas," *IEEE Trans. Antennas Propag.*, vol. 68, no. 6, pp. 4208–4217, Jun. 2020.

[23] L. Sun, Y. Li, and Z. Zhang, "Decoupling between extremely closely spaced patch antennas by mode cancellation method," *IEEE Trans. Antennas Propag.*, vol. 69, no. 6, pp. 3074–3083, Jun. 2021.

[24] T. Pei, L. Zhu, J. Wang, and W. Wu, "A low-profile decoupling structure for mutual coupling suppression in MIMO patch antenna," *IEEE Trans. Antennas Propag.*, vol. 69, no. 10, pp. 6145–6153, Oct. 2021.

[25] M. Abbasi, A. Aziz, W. Malik, A. Chishti, and R. Hussain, "A simple and modular MIMO antenna system for closely spaced patch antennas," *Microw. Opt. Techn. Lett.*, vol. 64, no. 7, pp. 1210–1216, Mar. 2022.

[26] J.-D. Zhang, L. Zhu, Q.-S. Wu, N.-W. Liu, and W. Wu, "A compact microstrip-fed patch antenna with enhanced bandwidth and harmonic suppression," *IEEE Trans. Antennas Propag.*, vol. 64, no. 12, pp. 5030–5037, Dec. 2016.

[27] S. Blanch, J. Romeu, and I. Corbella, "Exact representation of antenna system diversity performance from input parameter description," *Electron. Lett.*, vol. 39, no. 9, pp. 705–707, May 2003.

[28] M. Manteghi and Y. Rahmat-Samii, "Multiport characteristics of a wide-band cavity backed annular patch antenna for multipolarization operations," *IEEE Trans. Antennas Propag.*, vol. 53, no. 1, pp. 466–474, Jan. 2005.

[29] K. Ogawa, T. Matsuyoshi, and K. Monma, "An analysis of the performance of a handset diversity antenna influenced by head, hand and shoulder effects at 900 MHz: Part I—Effective gain characteristics," *IEEE Trans. Veh. Technol.*, vol. 50, no. 3, pp. 830–844, May 2001.

[30] J. H. Winters, "The diversity gain of transmit diversity in wireless systems with Rayleigh fading," *IEEE Trans. Veh. Technol.*, vol. 47, no. 1, pp. 119–123, Feb. 1998.

[31] H. Shin and J. H. Lee, "Capacity of multiple-antenna fading channel: Spatial fading correlation, double scattering, and keyhole," *IEEE Trans. Inf. Theory*, vol. 49, no. 10, pp. 2636–2647, Oct. 2003.

[32] H. Nguyen-Manh, D.-P. Pham, G. Nguyen-Hoai, H.-H. Tran, and N. Q. Dinh, "A design of MIMO antenna with high isolation and compact size characteristics," *IEEE Access*, vol. 11, pp. 93948–93955, 2023.

[33] H.-H. Tran, T. T.-L. Nguyen, H.-N. Ta, and D.-P. Pham, "Coupling reduction of extremely closely spaced circularly polarized MIMO patch antenna by phase shift method," *IEEE Access*, vol. 11, pp. 65347–65353, 2023.